



Ag₂CrO₄/g-C₃N₄/graphene oxide ternary nanocomposite Z-scheme photocatalyst with enhanced CO₂ reduction activity



Difa Xu^{a,b}, Bei Cheng^a, Weikang Wang^a, Chuanjia Jiang^{a,*}, Jiaguo Yu^{a,*}

^a State Key Laboratory of Advanced Technology for Materials Synthesis and Processing, Wuhan University of Technology, Wuhan 430070, PR China

^b Hunan Key Laboratory of Applied Environmental Photocatalysis, Changsha University, Changsha 410022, PR China

ARTICLE INFO

Keywords:

g-C₃N₄
Ag₂CrO₄
Graphene oxide
Photocatalytic CO₂ conversion
Z-scheme

ABSTRACT

Graphitic carbon nitride (g-C₃N₄)-based photocatalysts holds great promise on photocatalytic CO₂ conversion into solar fuels; however, the efficiency of pristine g-C₃N₄ is currently limited by its poor visible light absorption and rapid charge recombination. Employing silver chromate (Ag₂CrO₄) nanoparticles as photosensitizer and graphene oxide (GO) as cocatalyst, a novel ternary Ag₂CrO₄/g-C₃N₄/GO composite photocatalyst was fabricated for photocatalytic CO₂ reduction into methanol (CH₃OH) and methane (CH₄). The ternary composites exhibited an enhanced CO₂ conversion activity with a turnover frequency of 0.30 h⁻¹, which was 2.3 times that of pristine g-C₃N₄ under simulated sunlight irradiation. The enhanced photocatalytic activity was due to broadened light absorption, higher CO₂ adsorption and more efficient charge separation. Specifically, due to the matched band structure and appropriate loading ratio of Ag₂CrO₄, a direct Z-scheme Ag₂CrO₄/g-C₃N₄ heterojunction is formed, driven by the internal electric field across the Ag₂CrO₄/g-C₃N₄ interface. The formation of the direct Z-scheme heterojunction is substantiated by radical scavenging experiments and density functional theory calculations, and it benefits the photocatalytic reaction by accelerating the charge separation and improving the redox ability. Furthermore, GO cocatalyst not only promotes the charge transfer but also provides plentiful CO₂ adsorption and catalytic sites. This work exemplifies the facile development of ternary g-C₃N₄-based photocatalysts with high CO₂-conversion activity by coupling a small amount of Ag-based photosensitizer and metal-free cocatalyst.

1. Introduction

Harvesting sunlight to reduce carbon dioxide (CO₂) into organic fuels is a considerable approach for CO₂ conversion, which holds a promise to simultaneously address the environmental and energy issues [1–4]. However, CO₂ reduction involves the C–O bond cleavage and C–H bond formation, which can hardly be achieved under mild conditions because of the huge bond dissociation energy (127 kcal/mol) required for these reactions. Fortunately, CO₂ reduction can be driven by semiconductor photocatalysis, which can convert light into chemical energy and lower the activation barrier of CO₂ reduction. Many semiconductor photocatalysts are being developed for CO₂ conversion, including metal oxides, sulfides, phosphides and metal-free polymers [5–7]. Especially, graphitic carbon nitride (g-C₃N₄), a visible light-responsive polymer, has attracted considerable attention because of the characteristic layered structure, high chemical and thermal stabilities, low cost and easy preparation [8–13]. The conduction band (CB) level of bulk g-C₃N₄ is approximately –1.3 eV (versus normal hydrogen electrode, NHE, at pH 7), which is sufficiently negative to convert CO₂

into solar fuels, such as formic acid (HCOOH, with a standard redox potential of –0.61 eV), formaldehyde (HCHO, –0.48 eV), methanol (CH₃OH, –0.38 eV) and methane (CH₄, –0.24 eV), endowing g-C₃N₄ with a huge potential for solar CO₂ conversion.

However, CO₂ conversion rate of pristine g-C₃N₄ is typically very low and mainly limited by two factors, the inadequate visible light absorption due to the moderate band gap (E_g , ~2.7 eV) and the low quantum efficiency arising from the rapid charge recombination. For the purpose of CO₂ conversion efficiency improvement, a prevalent strategy is coupling g-C₃N₄ with a second semiconductor, photosensitizers and/or cocatalyst to construct a multi-component composite photocatalyst. In our previous study, silver chromate (Ag₂CrO₄) has proved a promising photosensitizer because its narrow band gap (~1.8 V) might favor the light absorption of g-C₃N₄ [14–16]. Moreover, as a semiconductor, Ag₂CrO₄ might also couple with g-C₃N₄ to form a binary heterojunction to promote the photogenerated charge separation. For example, it is reported that binary Ag₂CrO₄/g-C₃N₄ composites show higher photocatalytic activity and stability towards organic pollutant degradation than unitary Ag₂CrO₄ and g-C₃N₄ [17–21]. It is

* Corresponding authors.

E-mail addresses: jiangcj2016@whut.edu.cn (C. Jiang), yujiaguo93@whut.edu.cn (J. Yu).

also reported that Ag_2CrO_4 and $\text{g-C}_3\text{N}_4$ can form a Z-scheme heterojunction, which exhibits broadened light absorption range, better charge separation performance and stronger redox ability than traditional heterojunction, such as type-II heterojunction [19–22]. Nevertheless, these previous studies tend to evaluate the photocatalytic activity of $\text{Ag}_2\text{CrO}_4/\text{g-C}_3\text{N}_4$ composites by pollutant degradation, the efficiency of which might be controlled by either photocatalytic oxidation or reduction (or even both). As a result, the photogenerated charge separation approaches between Ag_2CrO_4 and $\text{g-C}_3\text{N}_4$ are still in dispute. To substantiate the Z-scheme charge transfer mechanism of $\text{Ag}_2\text{CrO}_4/\text{g-C}_3\text{N}_4$ composites, additional experimental and theoretical investigations are necessary.

For binary $\text{Ag}_2\text{CrO}_4/\text{g-C}_3\text{N}_4$ composites, there is still a limitation that the separated charges are difficult to transfer and participate in redox reactions [23]. To overcome this limitation, it is feasible to construct a ternary composite system by further introducing cocatalyst, which can provide the efficient redox reaction sites, inhibit the possible charge recombination and lower the reaction activation energy. The most widely used cocatalyst is platinum (Pt), which can improve CO_2 conversion activity and influence the product selectivity of $\text{g-C}_3\text{N}_4$ [24]. Meanwhile, graphene materials, including graphene oxide (GO) and reduced graphene oxide (rGO), are well known as efficient cocatalysts for $\text{g-C}_3\text{N}_4$ due to their superior electron mobility, two-dimensional (2D) layered structure, large surface area and perfect chemical stability. These characteristics make graphene an excellent metal-free cocatalyst alternative to the expensive noble metal Pt. Indeed, ternary composites containing graphene and $\text{g-C}_3\text{N}_4$ have been reported with enhanced charge transfer rates and photocatalytic activities, such as $\text{BiOI}/\text{g-C}_3\text{N}_4/\text{GO}$ [25], $\text{ZnO}/\text{g-C}_3\text{N}_4/\text{GO}$ [26], $\text{CdS}/\text{g-C}_3\text{N}_4/\text{rGO}$ [27], $\text{WO}_3/\text{g-C}_3\text{N}_4/\text{rGO}$ [28], $\text{Bi}_2\text{WO}_6/\text{g-C}_3\text{N}_4/\text{rGO}$ [29] and $\text{TiO}_2/\text{rGO}/\text{g-C}_3\text{N}_4$ [30]. Expectedly, the photocatalytic activity of binary composites can be further improved by employing graphene as cocatalyst.

Herein, we report the self-assembly fabrication of ternary $\text{Ag}_2\text{CrO}_4/\text{g-C}_3\text{N}_4/\text{GO}$ composite photocatalysts with high CO_2 -conversion activity under simulated sunlight irradiation. Although binary $\text{Ag}_2\text{CrO}_4/\text{g-C}_3\text{N}_4$ composites have been reported for organic pollutant degradation, there is little research on the ternary $\text{Ag}_2\text{CrO}_4/\text{g-C}_3\text{N}_4/\text{GO}$ composites and their photocatalytic CO_2 conversion activity, to our best knowledge. Ag_2CrO_4 with narrow band gap is employed as semiconductor photosensitizers to harvest light and promote the charge separation. Meanwhile, GO functions as electron collectors to promote the charge transfer and provides reactive sites for CO_2 conversion. The enhanced photocatalytic CO_2 conversion activity of the composite strongly suggests the formation of a Z-scheme heterojunction, which is carefully discussed in this work based on the experimental results and theoretical calculation. This work highlights a simple way to enhance the photocatalytic activity of $\text{g-C}_3\text{N}_4$ towards solar CO_2 conversion by coupling with Ag_2CrO_4 and GO, and affords an ideal example for developing similar ternary composite photocatalysts with high photocatalytic activity.

2. Experimental section

All reagents were supplied by Shanghai Chemical Reagent Factory (Shanghai, China) and used without further purification. Deionized (DI) water was used in this work.

2.1. Sample preparation

2.1.1. Pristine $\text{g-C}_3\text{N}_4$ and GO sheets

Pristine $\text{g-C}_3\text{N}_4$ was synthesized from urea in a covered alumina crucible at 520 °C for 2 h (at 5 °C min⁻¹) and labelled as CN. GO was produced from the oxidation of graphite powers (3 g, > 99.8%), which were previously oxidized by concentrated H_2SO_4 (15 mL), $\text{K}_2\text{S}_2\text{O}_8$ (2.5 g) and P_2O_5 (2.5 g) mixtures at 80 °C for 8 h and then oxidized according to Hummers and Offeman methods. Suspensions of $\text{g-C}_3\text{N}_4$

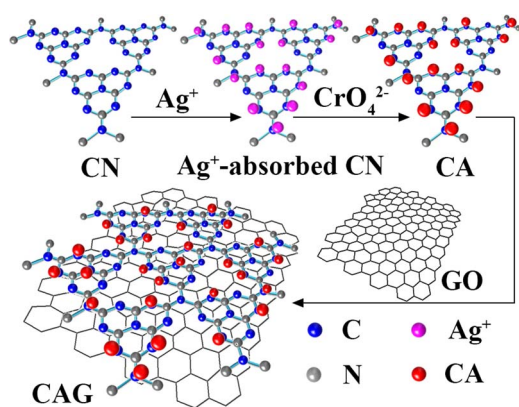


Fig. 1. Schematic illustration of CA and CAG composite fabrication.

and GO were prepared by respectively dispersing $\text{g-C}_3\text{N}_4$ (500 mg) and GO (100 mg) power into water (100 mL) and subsequent ultrasonic exfoliation for 12 h.

2.1.2. Pristine Ag_2CrO_4 particles

Pristine Ag_2CrO_4 particles were obtained from simple precipitation method and labelled as AO. Briefly, K_2CrO_4 solution (100 mL, 0.03 mol L⁻¹) was dripped into AgNO_3 solution (100 mL, 0.06 mol L⁻¹) with strong stirring for 1 h.

2.1.3. Binary $\text{Ag}_2\text{CrO}_4/\text{g-C}_3\text{N}_4$ and ternary $\text{Ag}_2\text{CrO}_4/\text{g-C}_3\text{N}_4/\text{GO}$ composites

The composites were fabricated by self-assembly precipitation method (Fig. 1). Typically, a known volume of AgNO_3 solution (0.06 mol L⁻¹) was added into the $\text{g-C}_3\text{N}_4$ suspension (5 mg mL⁻¹) and stirred for 12 h, $\text{Ag}_2\text{CrO}_4/\text{g-C}_3\text{N}_4$ composites were obtained by slowly dripping the same volume of K_2CrO_4 solution (0.03 mol L⁻¹) into the mixture and then stirring for 2 h. For determining the optimal Ag_2CrO_4 loading ratio, samples with different theoretical weight ratios of Ag_2CrO_4 to $\text{g-C}_3\text{N}_4$ (5, 10, 20, 30 and 40 wt%) were prepared and labelled as CAx ($x = 5, 10, 20, 30$ and 40). Among them, the CA10 sample exhibited the best photocatalytic activity (shown below in Section 3.3 Photocatalytic Activity and Stability) and was specially labelled as CA. Subsequently, a known amount of GO solution (1.0 mg mL⁻¹) was added to CA aqueous suspension and stirred for 12 h to obtain the ternary $\text{Ag}_2\text{CrO}_4/\text{g-C}_3\text{N}_4/\text{GO}$ composite, which was labelled as CAG.

2.1.4. Binary $\text{g-C}_3\text{N}_4/\text{GO}$ composites

According to the previous reports that the ideal loading amount of graphene to $\text{g-C}_3\text{N}_4$ was 1 wt% [31], this weight ratio of GO to $\text{g-C}_3\text{N}_4$ was also employed in this work. A mixture suspension of GO (1 mL, 1 mg L⁻¹) and $\text{g-C}_3\text{N}_4$ (100 mL, 5 mg L⁻¹) was treated under ultrasonication for 12 h and labelled as CG. Meanwhile, Ag-loaded $\text{g-C}_3\text{N}_4$ (Ag-CN) with 10 wt% ratio of Ag to $\text{g-C}_3\text{N}_4$ was prepared by photo-reduction method as a control sample [32]. All samples were washed with water and dried in an oven at 80 °C.

2.2. Characterization

The specified characterization description is provided. For example, The crystal phase of the products was studied by X-ray diffraction (XRD) on a D/Max-RB X-ray diffractometer (Rigaku, Japan), using the wavelength of $\text{Cu K}\alpha$ radiation ($\lambda = 1.54056$ nm) operated at 40 kV and 80 mA with a scan rate (20) of 0.05° s⁻¹. Field emission scanning electron microscopy (FESEM) and the corresponding elemental mapping images were obtained by a JSM-7500F cold-field emission scanning electron microscope (JEOL, Japan) at an accelerating voltage of 5 and 10 kV, respectively. Transmission electron microscopy (TEM) images were obtained by a JEM-2100F electron microscope (JEOL,

Japan) at an accelerating voltage of 200 kV. Fourier transform infrared (FTIR) spectra were recorded with a Nicolet iS50 spectrometer (Thermo Scientific, USA). Zeta potential was measured on a ZS90 zetasizer (Malvern, UK). The nitrogen (N_2) adsorption-desorption isotherms and CO_2 adsorption isotherms were respectively measured by an ASAP 2020 and ASAP 3020 N_2 adsorption apparatus (Micromeritics Instruments, USA). The CO_2 adsorption measurement was carried out at 25 °C. UV/Vis absorption spectra were measured with a UV2600 UV-vis spectrophotometer (Shimadzu, Japan). X-ray photoelectron spectroscopy (XPS) and valence band (VB) XPS spectra measurements were performed on a VG ESCALAB 210 spectrometer with a stand Mg K α excitation source (1253.6 eV) under a vacuum pressure $< 10^{-6}$ Pa, and the binding energies were referenced to the C 1s peak at 284.6 eV of adventitious carbon. Photoluminescence (PL) spectra were measured on an F-7000 fluorescence spectrophotometer (Hitachi, Japan).

2.3. Time-resolved transient PL measurement

Time-resolved transient PL decay curves were measured on a FLS920 fluorescence spectrophotometer (Edinburgh Instruments, UK) under the excitation of 325 nm. The emission decay data were fitted to a double-exponential model and the emission decay behavior is deduced through Eq. (1):

$$\langle \tau \rangle = \frac{A_1 \tau_1^2 + A_2 \tau_2^2}{A_1 \tau_1 + A_2 \tau_2} \quad (1)$$

where τ and A are the decay time and the relative magnitude of components, respectively, and $\langle \tau \rangle$ is the intensity-averaged lifetime used for an overall comparison. The fitting results show the fast decay component (τ_1 and A_1) and the minority-slow component (τ_2 and A_2), decaying from the free excited states and the bound excited states, respectively.

2.4. Photoelectrochemistry measurement

Photocurrent density versus time ($i-t$) curves was measured on a CHI660C electrochemical workstation (Chenhua Instruments, China). The test system comprised a working electrode (obtained from samples fixed on fluorinated tin oxide (FTO) glass using the doctor-blade technique, 1.5 cm² active area), a Pt counter electrode, a Ag/AgCl reference electrode and KNO_3 electrolyte (0.5 M). The visible light was provided by a low power LED (3 W, 420 nm) light (Shenzhen LAMPLIC Science Co.,Ltd., China). The same test system was used for Mott-Schottky (MS) measurement but in the dark. The scan rate was 25 mV/s and the scan frequency was 1 kHz.

2.5. Photocatalytic activity measurement

A 300-W Xe arc lamp (Changzhou Siyu, China) was employed as simulated sunlight source with (visible light) or without (full light spectrum) 420 nm cut-off filters. A 200-mL customized glass flask with double neck was employed as reactor. First, the sample (100 mg) was added to the reactor, dispersed in water (10 mL) and dried at 80 °C to prepare a coating film on the bottom of the reactor. Second, $NaHCO_3$ (120 mg) was added to the neck of the reactor and followed by continuous nitrogen blowing (30 min) to ensure the anaerobic reaction conditions. Third, HCl (0.25 mL, 4 mol L⁻¹) was injected into the neck of reactor and reacted with $NaHCO_3$ to produce CO_2 and H_2O gases. The reactor was kept in the dark for 1 h to achieve adsorption-desorption equilibrium between CO_2 and sample, and then the reactor was placed under light irradiation for 1, 2 and 3 h, respectively. The photocatalytic conversion products were detected by a gas chromatograph (GC-2014C, Shimadzu) equipped with a flame ionization detector. To investigate the stability of the ternary $Ag_2CrO_4/g-C_3N_4/GO$ composites on CO_2 conversion, the samples were collected after each photocatalytic

reduction reaction for 3 h and recycled for 6 runs according to the same procedure.

2.6. Radical scavenger measurement

To find out the predominant reactive species participating in photocatalytic degradation, Ethylene diamine tetraacetic acid (EDTA, 0.01 M), *p*-benzoquinone (BZQ, 0.1 mM) and isopropanol (IPA, 0.1 M) were used as scavengers for photogenerated holes (h_{VB}^+), superoxide radicals ($\cdot O_2^-$) and hydroxyl radicals ($\cdot OH$), respectively. Typically, the photocatalyst (20 mg) was dispersed in methylene blue (MB) aqueous solution (50 mL, 1×10^{-5} mol L⁻¹) with or without scavengers and then stirred in the dark for 1 h. Subsequently, the MB solution was irradiated by visible light and about 4 mL suspension was taken out every 5 min. After the separation by centrifugation (4500 rpm, 15 min) and filtration through 0.4 μ m filter membrane, the residual concentration of MB solution was determined by its absorbance at 663 nm. The apparent rate constant (k) was calculated from kinetic equation $\ln(C_0/C_t) = kt$, where t was the sampling time, C_0 and C_t were the initial and residual MB concentration before and after photocatalytic reaction, respectively.

2.7. DFT calculation

The first-principles calculations were based on density functional theory (DFT), using plane-wave pseudopotential method as implemented in the Cambridge Sequential Total Energy Package (CASTEP) code. The exchange–correlation function was described by the generalized gradient approximation (GGA) with Perdew–Burke–Ernzerhof (PBE) functionals. The interaction between valence electron and ionic core was defined by the ultrasoft pseudopotential. The plane wave basis set of 340 eV was used as the kinetic cutoff energy, the $4 \times 4 \times 2$ k -points were employed to set Monkhorst–pack grids for both Ag_2CrO_4 and $g-C_3N_4$ models. The convergence parameter of geometric optimization for energy change, maximum force, maximum pressure and maximum displacement were 2×10^{-5} eV per atom for total energy, 0.03 eV Å⁻¹, 0.05 GPa and 0.001 Å, respectively. When the total tolerance was smaller than 1×10^{-6} eV per atom, the self-consistent calculations were finished. The band structures of Ag_2CrO_4 and $g-C_3N_4$ could be obtained after the geometric optimization achievement, which were also used to determine the effective masses of charge carriers of Ag_2CrO_4 and $g-C_3N_4$.

The effective masses of electrons ($m^* e$) and holes ($m^* h$) of semiconductors respectively around CB minimum (CBM) and VB maximum (VBM) were calculated according to Eq. (2).

$$m^* = \pm \hbar^2 \left(\frac{d^2 E_k}{dk^2} \right)^{-1} \quad (2)$$

where m^* is the effective mass of charge carriers, \hbar is the reduced Planck constant, k is the wave vector, and E_k is the band edge energy as a function of wave vector k .

3. Results and discussion

3.1. Phase structure and morphology

According to XRD patterns shown in Fig. 2a, pristine $g-C_3N_4$ (sample CN) and Ag_2CrO_4 (sample AO) are hexagonal phase (JCPDS No. 87-1526) and orthorhombic structure (JCPDS No. 26-0952), respectively. The XRD spectra of the CA and CAG composites generally resemble that of $g-C_3N_4$, but some peaks belonging to the (220), (031), (211) and (002) crystal planes of Ag_2CrO_4 are also observed, suggesting the co-existence of Ag_2CrO_4 and $g-C_3N_4$ in these composites. Meanwhile, the peak intensity of Ag_2CrO_4 in composites is very weak, indicating the low crystallinity and/or small size of Ag_2CrO_4 particles [33]. However,

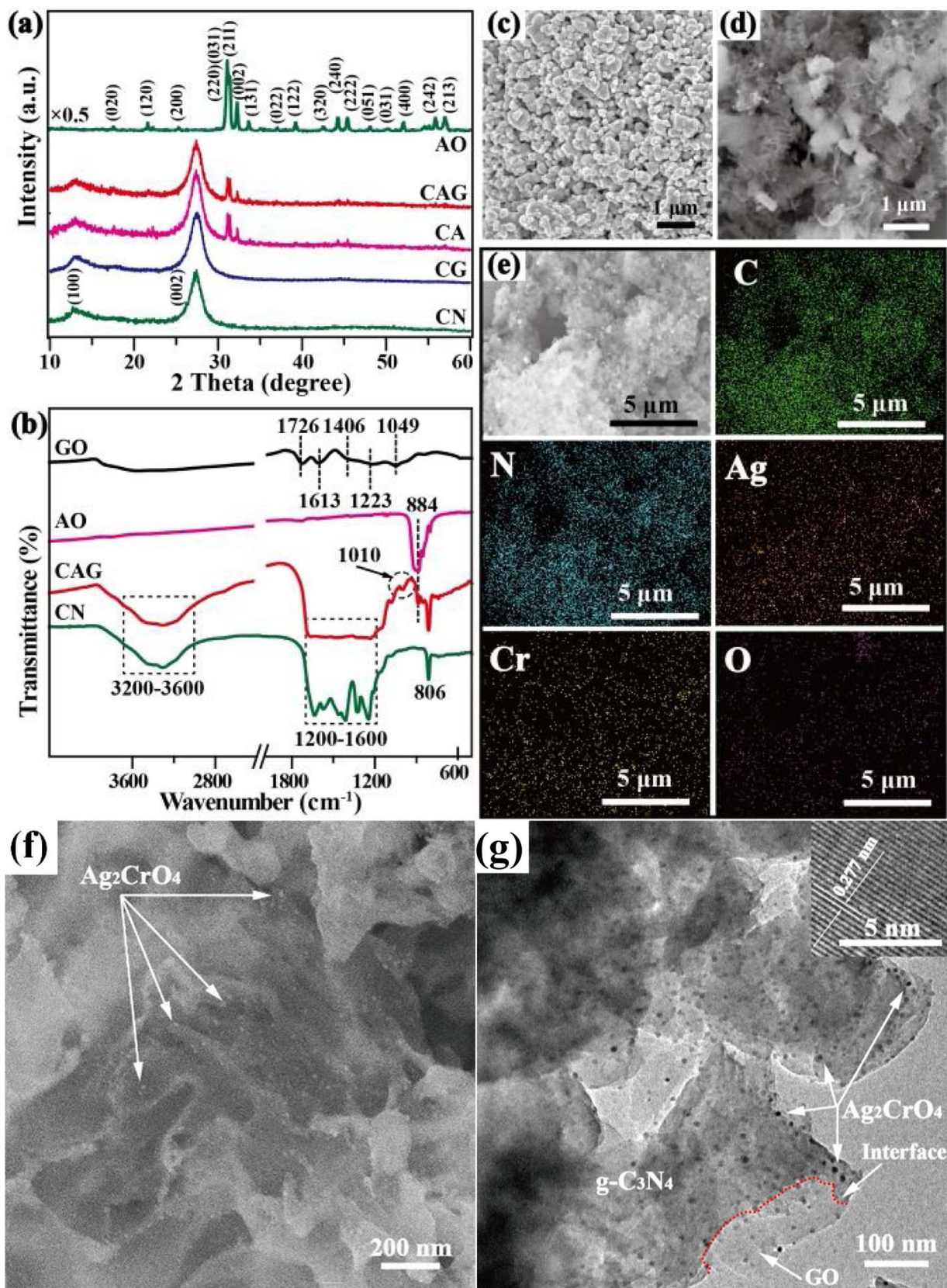


Fig. 2. (a) XRD patterns and (b) FTIR spectra of the obtained samples; SEM images of (c) Ag_2CrO_4 and (d) $\text{g-C}_3\text{N}_4$, (e) the corresponding element mapping images of CAG composites at low-magnification, (f) SEM and (g) TEM images of CAG composites at high magnification. Inset of part g presents the high-resolution TEM image of Ag_2CrO_4 particles in sample CAG.

no diffraction peaks of GO can be seen for the CG and CAG composites due to the relatively low amount and diffraction intensity of GO. The chemical structure is further proved by FTIR spectra (Fig. 2b). Pristine g-C₃N₄ shows three main absorption regions at 3200–3600 cm^{−1} (H₂O and N–H band), 1600–1200 cm^{−1} (CN heterocycles) and 806 cm^{−1} (the condensed CN heterocycles) [24]. The peak of pristine Ag₂CrO₄ at ~884 cm^{−1} corresponds to Cr–O stretching vibrations of CrO₄^{2−} groups [34]. Some peaks at 1049 cm^{−1} (alkoxy C–O), 1223 cm^{−1} (epoxy C–O–C), 1406 cm^{−1} (tertiary C–OH), 1620 cm^{−1} (aromatic C=C) and 1726 cm^{−1} (carboxyl C=O) are attributed to oxygen function groups of GO [31]. The FTIR spectrum of CAG resembles that of pristine g-C₃N₄, while it is difficult to identify the peaks for oxygen-containing groups of GO, because most of them highly overlap with those of g-C₃N₄. However, a minor peak at 1010 cm^{−1} relating to C–O (alkoxy) stretching vibrations can be observed, which is red shift with respect to pristine GO (1049 cm^{−1}). This is due to the redistribution of electron density between N–H and C–O groups, indicating the formation of hydrogen bonding between g-C₃N₄ and GO. Another minor peak at ~884 cm^{−1} further confirms the existence of Ag₂CrO₄ in the CAG composites.

Pristine Ag₂CrO₄ obtained from the precipitation method shows irregular morphology with an average particle size of 500 nm (Fig. 2c). Pristine g-C₃N₄ exhibits layered structures with many wrinkles and irregular folding sheets that might provide accessible sites for Ag₂CrO₄ particle growth (Fig. 2d). The elemental mapping images of sample CAG at low magnification clearly exhibit C, N, Ag, Cr and O elements with a uniform distribution (Fig. 2e), suggesting the coexistence of Ag₂CrO₄ and g-C₃N₄ in the composites. More detailed morphological information is given by SEM and TEM images at high magnification. Due to the heavier atomic mass of Ag and Cr than that of C and N, Ag₂CrO₄ tends to scatter the incident electrons more efficiently, and appears brighter in the SEM images but darker in the TEM images than g-C₃N₄ [35,36]. Meanwhile, GO can be distinguished from g-C₃N₄ because the former has the thinner layer structure and looks more transparent than the latter in the TEM images. As shown in Fig. 2, large amounts of brighter Ag₂CrO₄ nanoparticles deposit on the g-C₃N₄ sheets. This can be further confirmed by TEM images (Fig. 2g), in which darker Ag₂CrO₄ nanoparticles with a lattice spacing of 0.277 nm (inset of Fig. 2g) are highly dispersed on the surface of g-C₃N₄ sheets. Moreover, an obvious interface (indicated by red dot line) between g-C₃N₄ and GO is observed, suggesting their compact lamellar stacking, which is good for fast interfacial charge transfer [37].

The surface chemical compositions of the obtained samples are investigated by XPS characterization. The survey spectrum of the CA sample shows not only Ag, Cr and O elements belonging to Ag₂CrO₄ but also C and N elements of g-C₃N₄ (Fig. 3a). Only one C 1s peak (284.6 eV) resulting from contaminant hydrocarbon can be observed for AO sample, whereas the g-C₃N₄ sample shows another peak at 288.1 eV corresponding to C in C–N groups, which negatively shifts to 287.8 eV for the CA sample (Fig. 3b). N 1s XPS spectrum of pristine g-C₃N₄ can be fitted into three peaks at 398.6 eV (sp²-bonded N atoms, C=N=C), 400.0 eV (ternary N groups, N–(C)₃) and 401.2 eV (side N–H groups) [38]. For the CA sample, the peak at 398.6 eV negatively shifts to 398.3 eV, while the one at 401.2 eV disappeared (Fig. 3c). The disappearance of this peak is due to the strong interaction between Ag⁺ and N–H groups, such as –NH₂ and –NH–, which are located at the surface of the g-C₃N₄ sheets and function as important growth sites of Ag₂CrO₄ crystal nuclei [9]. The Ag 3d spectrum of pristine Ag₂CrO₄ can be separated into two groups, one group at 367.5 and 373.5 eV respectively corresponding to Ag 3d_{5/2} and Ag 3d_{3/2} of Ag⁺, and the other group at 368.4 eV (Ag 3d_{5/2}) and 374.4 eV (Ag 3d_{3/2}) assigned to metallic Ag (Ag°) [15] (Fig. 3e). It is not surprising that there is Ag° in pristine Ag₂CrO₄, due to its good photosensitivity and serious photo-corrosion feature [16]. However, only one group (at 367.8 and 373.8 eV) belonging to Ag⁺ is observed for the CA composite, indicating that the photocorrosion of Ag₂CrO₄ particles is inhibited after

coupling with g-C₃N₄. A doublet Cr 2p peak of pristine Ag₂CrO₄ at 578.3 eV (Cr 2p_{3/2}) and 587.5 eV (Cr 2p_{1/2}) is attributed to Cr⁶⁺ [21], which is positively shifted to 578.5 and 587.7 eV for the CA composite, respectively (Fig. 3e). Meanwhile, the other peak at about 572.1 eV is assigned to Ag 3p signal and is also positively shifted to 572.4 eV for CA composites [21]. The O 1s peak at 529.5 eV of pristine Ag₂CrO₄ corresponds to its lattice oxygen, which is positively shifted to 529.8 eV for the CA composite, and the other peaks at about 531.3 and 531.4 eV ascribe to the water species or external –OH group chemisorbed on the surface of Ag₂CrO₄ and CA composite, respectively [19,21]. It is noteworthy that the binding energies of C and N elements of the CA composite are slightly lower than those of pristine g-C₃N₄, while binding energies of Ag, Cr and O elements are slightly positively shifted compared with pristine Ag₂CrO₄. Similar phenomena are widely reported in g-C₃N₄-based photocatalysts such as ZnO/g-C₃N₄, Ag₂CrO₄/g-C₃N₄, Ag₃VO₄/g-C₃N₄ and BiPO₄/g-C₃N₄ composites [19,39–41]. The binding energy shift indicates the strong interaction between Ag₂CrO₄ nanoparticles and g-C₃N₄ sheets [42]. This is mainly due to the π-back-bonding interaction from unoccupied orbital of Ag 5s5p and Cr 3d to π electrons of g-C₃N₄ and lone pair electrons of N atom [5].

Interestingly, the particle size of Ag₂CrO₄ in the CAG composite is very small, and similar results have been observed in the previous reports [18,19,43,44]. Due to the incomplete polymerization reaction, there are some residual N–H groups on the surface of g-C₃N₄, providing sites to chemically adsorb Ag⁺ through coordination bond. After slowly introducing CrO₄^{2−}, the crystal nuclei of Ag₂CrO₄ nanoparticles are formed on the surface of g-C₃N₄. The layered g-C₃N₄ with many wrinkles not only provides accessible sites for Ag₂CrO₄ nucleus growth but also suppresses the particle aggregation due to the space limitation [45]. As a result, Ag₂CrO₄ particles with much smaller size are obtained and can be closely deposited on the surface of g-C₃N₄ sheets by Coulomb interaction. On the other hand, there are two types of interaction benefiting the strong lamellar stacking between g-C₃N₄ and GO. One is the π–π stacking interaction as a result of the similar sp² lattice structure of g-C₃N₄ and GO, and the other is the hydrogen bonding interaction ascribed to the edge nitrogen-containing groups of g-C₃N₄ and the oxygen-containing groups of GO [46,47]. The small particle size and the close contact interface mean a short migration distance of photo-generated charges, facilitating the fast charge separation and transfer [37,48–52].

3.2. Physicochemical and photoelectrochemistry properties

The optical absorption properties of the samples are presented in Fig. 4a and the absorption edges of pristine g-C₃N₄ and Ag₂CrO₄ are about 450 (E_g = 2.7 eV) and 700 nm (E_g = 1.8 eV), respectively. Compared with g-C₃N₄, the absorption edges of all composites have no significant shift, indicating that Ag₂CrO₄ and GO are not incorporated into the lattice of g-C₃N₄ [15]. The light absorption intensity of all composites is strengthened due to the photosensitization of Ag₂CrO₄ and/or GO, which is beneficial for the photocatalytic activity improvement. Among them, the CAG composite shows the best light absorption due to the dual photosensitization by Ag₂CrO₄ and GO. Notably, CG and CA composites exhibit different absorption in different wavelength region, depending on whether g-C₃N₄ is excited or not. When the wavelength is larger than 450 nm, g-C₃N₄ cannot be excited and the enhanced absorption mainly originates from the intrinsic absorption of Ag₂CrO₄ or GO, thus CG composites show higher absorption than CA composites due to the stronger intrinsic absorption of GO in visible light region. This can also be demonstrated by the color of the samples (inset of Fig. 4a), where the color of CG is darker than that of CA. However, at wavelengths shorter than 450 nm, both Ag₂CrO₄ and g-C₃N₄ are excited, and the absorption of the CA composite is higher than that of the CG composite, indicating an unusual transfer route of photoinduced charges between Ag₂CrO₄ and g-C₃N₄ [53].

The samples show N₂ adsorption-desorption isotherms of type IV

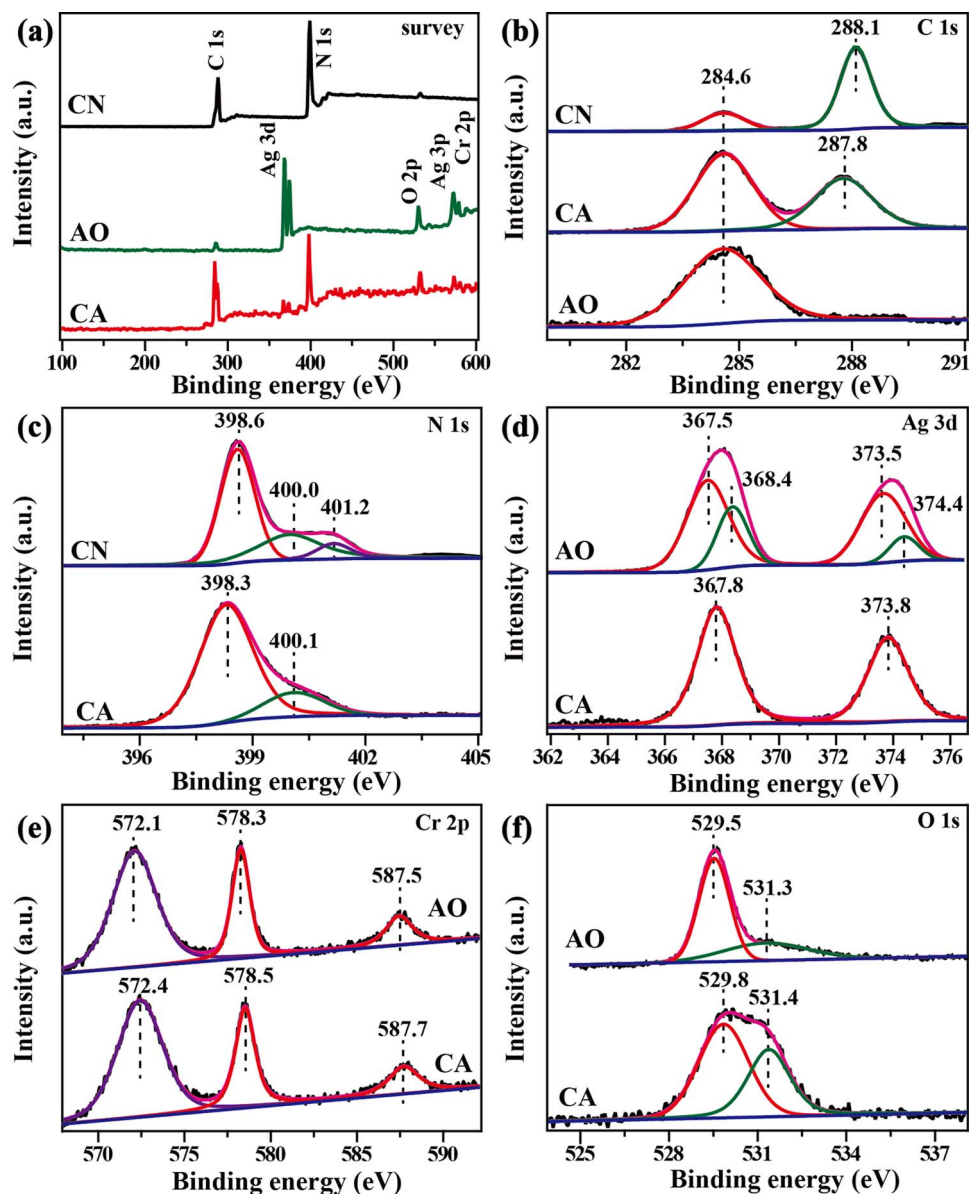


Fig. 3. (a) XPS survey spectra and the corresponding high-resolution XPS spectra of (b) C 1s, (c) N 1s, (d) Ag 3d, (e) Cr 2p and (f) O 1s of the obtained samples.

with the type H3 loop (Fig. 4b), suggesting the mesoporous structure induced by stacking of layered materials. This can be further demonstrated by the pore size distributions centred at 30–80 nm. The BET specific surface area of CN, CG, CA and CAG samples is 37, 36, 34 and 38 m²/g, respectively (Table 1), showing no obvious difference, due to the low amount of Ag₂CrO₄ and GO addition [54]. However, CO₂ adsorption capacities of the samples are different, and the binary and ternary composites show higher CO₂ adsorption capacity than pristine g-C₃N₄ (Fig. 4c). GO is helpful for the enhanced CO₂ adsorption based on the following facts: (1) the porous network structure of GO facilitating the rapid transportation of CO₂ molecules [55,56]; (2) a large 2D π -conjugated structure of GO and delocalized π -conjugated binding $\pi\text{-}\pi$ of CO₂ establishing the unique $\pi\text{-}\pi$ conjugation [57]; (3) functional groups of GO such as –COOH and –OH providing additional binding sites [58]. Especially, the ternary CAG composite exhibits the highest CO₂ adsorption (0.11 mmol g⁻¹) at 760 mmHg and 25 °C, implying the superior photocatalytic CO₂ reduction activity of the ternary composites.

The charge separation and transfer characteristics of the samples were compared by fluorescence spectroscopy and photocurrent

measurement. As shown in Fig. 4d, pristine g-C₃N₄ exhibited very strong steady-state PL intensity under an excitation wavelength of 375 nm, but the CG composite showed a decreased PL intensity, which was further decreased for CA, and the CAG composite had the weakest intensity. The steady-state PL intensity of the CG composite was weaker than that of pristine g-C₃N₄ because GO can serve as the electron acceptor inhibiting the charge recombination and facilitating the charge transfer. Surprisingly, the steady-state PL intensity of the CA composite was weaker than that of CG, implying an efficient charge separation and transfer between g-C₃N₄ and Ag₂CrO₄. The time-resolved transient PL spectra show that the order of intensity-averaged lifetime ($\langle \tau \rangle$) value was in line with the steady-state PL results (Fig. 4e). The pristine g-C₃N₄ sample showed the longest $\langle \tau \rangle$ value of 8.40 ns, which was decreased to 6.50 ns for the CAG composite. The shortened decay lifetime indicates a nonradiative pathway and prolonged lifetime of the photogenerated charge carriers [59–62], which increase the possibility of electrons selectively reducing CO₂ to CH₄ [63]. The photocurrent density of the samples followed the order of CN < CG < CA < CAG (Fig. 4f), suggesting enhanced charge separation and transfer after g-C₃N₄ coupling with both Ag₂CrO₄ and GO, which can significantly

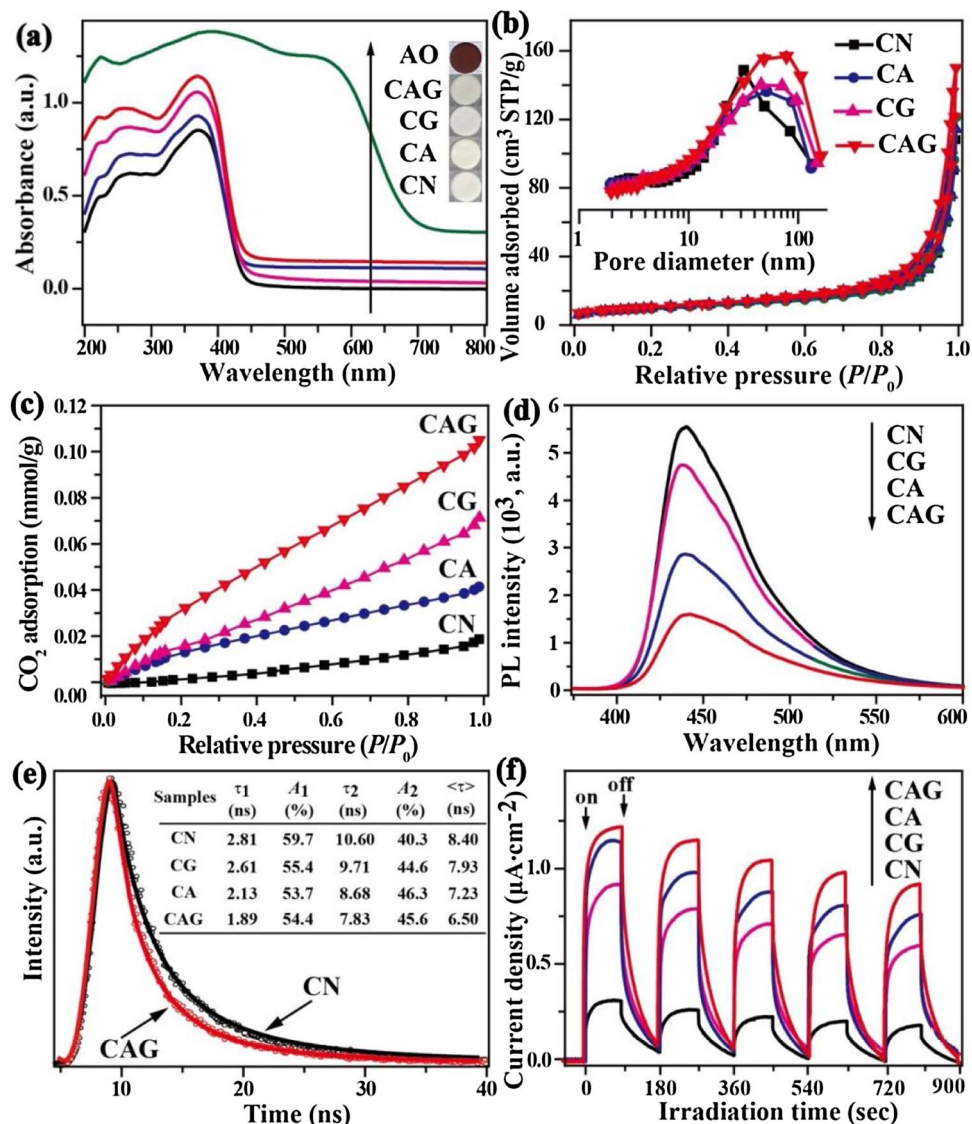


Fig. 4. (a) UV/Vis absorption spectra and the corresponding colors, (b) N₂ adsorption-desorption isotherms and pore-size distribution curves, (c) CO₂ adsorption isotherms, (d) steady-state PL spectra, (e) time-resolved transient fluorescence decay and the calculated average lifetime and (f) transient photocurrent response of the obtained samples.

Table 1
Textural properties and photocatalytic activity (expressed as TOF) of the samples.

Sample	Composition	S _{BET} (m ² /g)	Pore volume (cm ³ /g)	Pore size (nm)	TOF (s ⁻¹)
CN	g-C ₃ N ₄	37	0.10	10.8	0.13
CG	g-C ₃ N ₄ /GO	36	0.09	10.1	0.17
CA	Ag ₂ CrO ₄ /g-C ₃ N ₄	34	0.09	11.2	0.22
CAG	Ag ₂ CrO ₄ /g-C ₃ N ₄ /GO	38	0.11	12.1	0.30

promote CO₂ reduction reaction.

3.3. Photocatalytic activity and stability

In blank experiments without either photocatalysts or light, no reaction products can be detected, suggesting the necessity of both photocatalysts and light for CO₂ conversion. Meanwhile, no solar fuels are formed in the absence of CO₂, indicating CO₂ employed as the only carbon source in this experiment. No photocatalytic CO₂-conversion activity was observed for pristine Ag₂CrO₄, because the CB level of Ag₂CrO₄ is less negative than the redox potential of CO₂-conversion reaction. The CO₂-conversion rate of pristine g-C₃N₄ was relatively low

because of the poor light absorption and the rapid charge recombination. Interestingly, the CO₂-conversion activity was enhanced after coupling g-C₃N₄ with Ag₂CrO₄, and the composite with 10 wt% Ag₂CrO₄ exhibited the highest CH₃OH production; however, excessive Ag₂CrO₄ can cover the active sites of g-C₃N₄ and lead to a negative effect for CO₂ conversion (Fig. 5a).

Fig. 5b shows the CH₃OH and CH₄ production of CN, CG, CA and CAG composites under simulated sunlight irradiation for 1, 2 and 3 h, respectively. It was found that the solar fuel production increased with increasing irradiation time within 3 h. However, the production did not further increase when the irradiation time was prolonged to 4 h (not shown here). This might be due to the reaction balance between CO₂ reduction and product oxidation [49], the shielding of active sites by the increasing amounts of intermediates and the competition between by-product O₂ and carbon species for electrons. The resulting rate of hydrocarbon production in 3 h is then converted to TOF (n(hydrocarbon products) per n(melem units) per hour) according to g-C₃N₄ photocatalyst to compare their intrinsic activity [38,64]. Meanwhile, commercial TiO₂ P25 (Degussa, Germany) and Ag-loaded g-C₃N₄ (Ag-CN) were used as references (Fig. 5c). It is found that the CAG composite had the highest CO₂-conversion activity of 1.03 μmol g⁻¹ with a TOF value of 0.30 h⁻¹ for the first 3 h of full spectrum irradiation, which

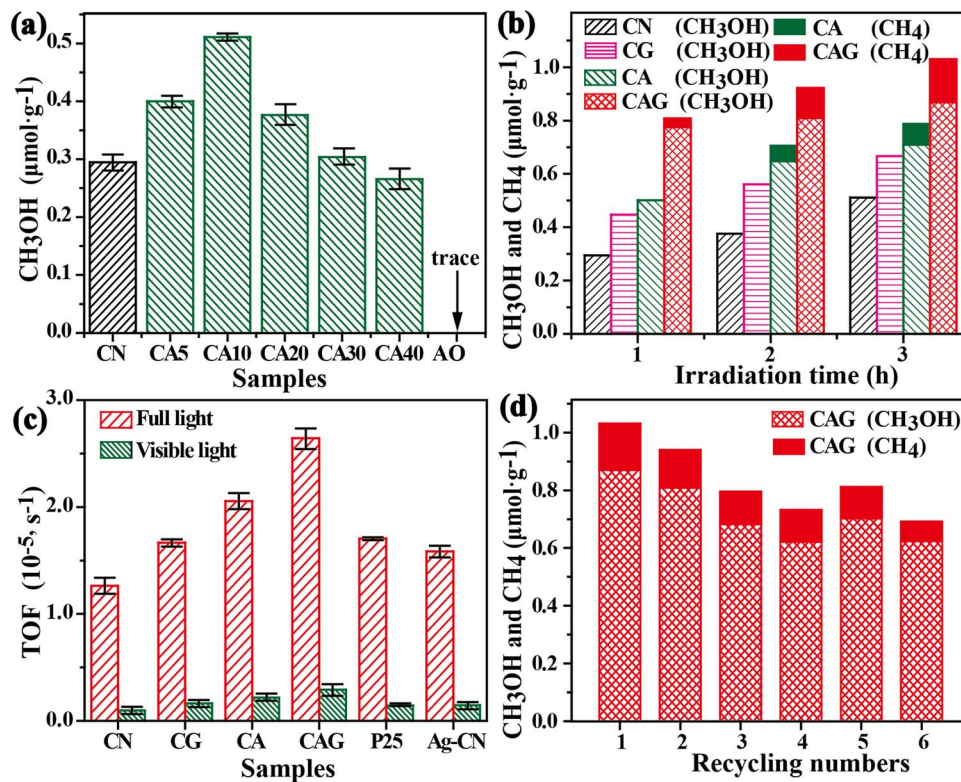


Fig. 5. (a) CH_3OH production of CN, CA_x ($x = 5, 10, 20, 30$ and 40) and AO samples under simulated sunlight irradiation for 1 h; (b) CH_3OH and CH_4 production of CN, CG, CA and CAG samples under full spectrum light irradiation for $1, 2$ and 3 h; (c) the calculated TOF of the obtained samples under full spectrum and visible light irradiation for 3 h, respectively; and (d) the recycling test results of CA composites on photocatalytic CO_2 reduction under simulated sunlight irradiation.

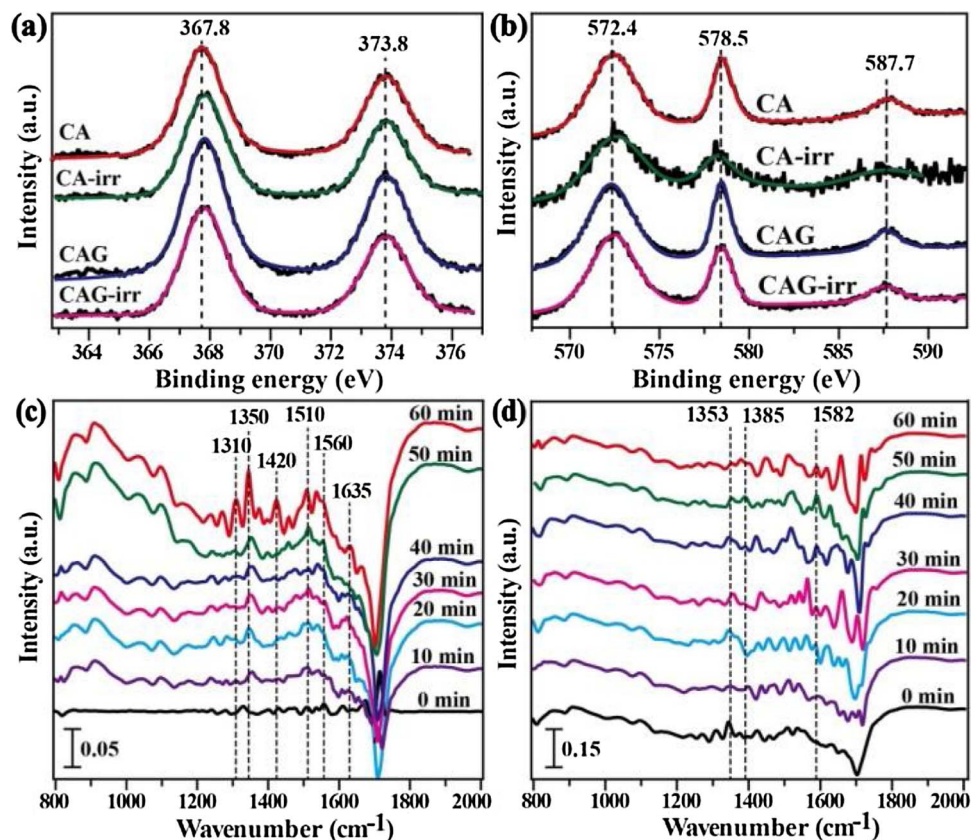


Fig. 6. The high-resolution XPS spectra of (a) Ag 3d and (b) Cr 2p of the obtained samples prior to (CA and CAG) and subsequent to (CA-irr and CAG-irr) photocatalytic reaction, and (c) in-situ FTIR spectra of CO_2 adsorption in the dark and (d) CO_2 reduction under 420 nm light irradiation on the CAG composites.

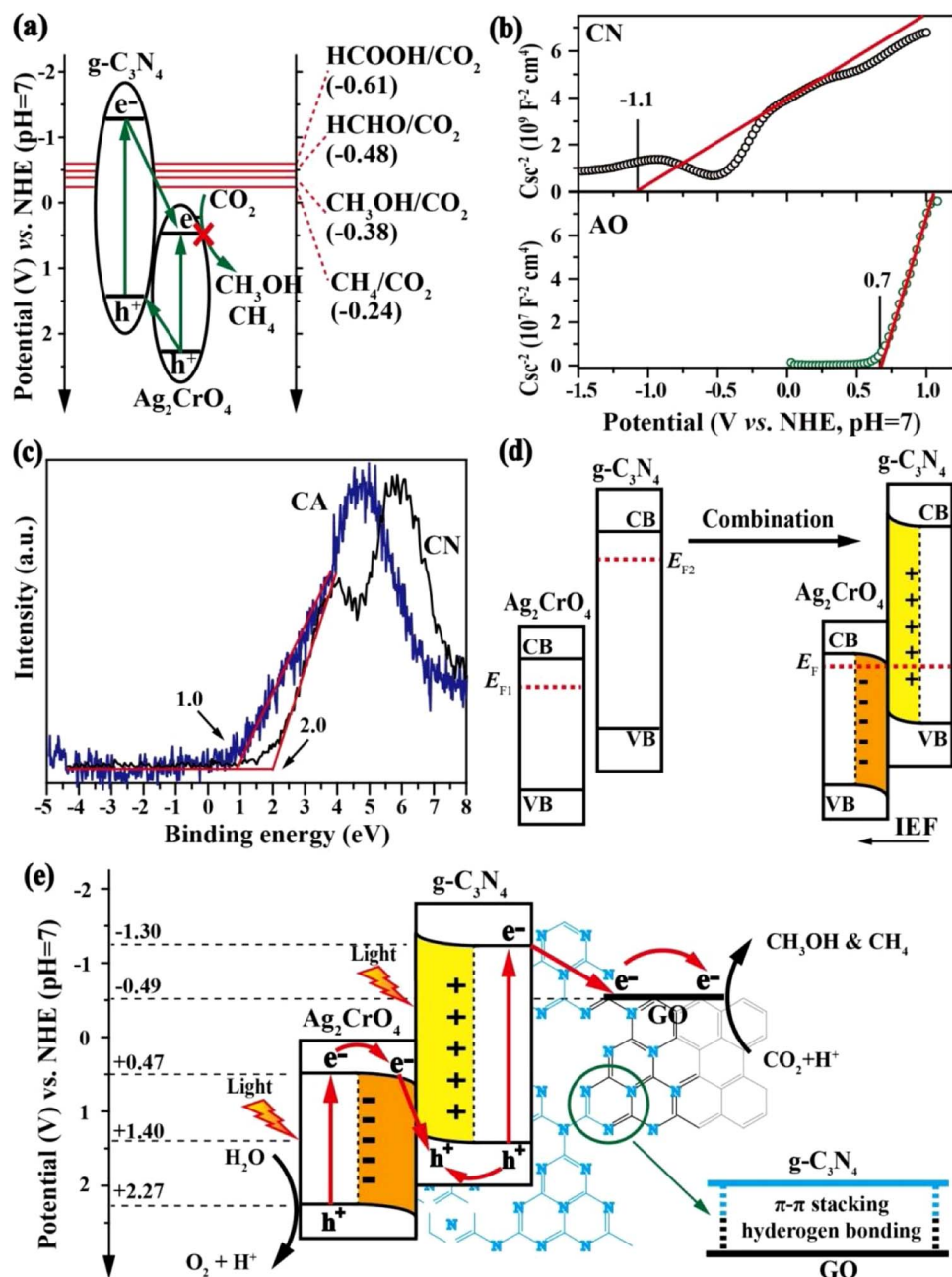


Fig. 7. (a) Hypothetical type-II heterojunction for CA composites, (b) Mott–Schottky plots of CN and AO samples, (c) VB XPS spectra of CN and CA samples, (d) internal electric field (IEF) formation after Ag_2CrO_4 and $\text{g-C}_3\text{N}_4$ combination, and (e) the proposed Z-scheme photocatalytic mechanism for the CAG composite.

is 2.3, 1.7, 1.3, 1.5 and 1.8 times that of CN, CG, CA, P25 and Ag-CN samples, respectively. Although metallic Ag loading improved the TOF value of pristine $\text{g-C}_3\text{N}_4$ from 0.13 to 0.17 h^{-1} , it was still lower than that of the CAG composite, indicating that the enhanced CO_2 -conversion rate is not fully due to Ag loading, and Ag_2CrO_4 plays important roles in CO_2 -conversion rate enhancement. However, compared to full spectrum light, the visible-light CO_2 -conversion rates of the samples were very low, which might relate to the weak absorption of visible light as confirmed in the absorption spectra (Fig. 4a). The photocatalytic stability of the CAG composite was evaluated by a six-time recycle test. As shown in Fig. 5d, the CH_3OH and CH_4 production of CAG composites slightly decreased over the first three cycles but changed little over the following cycles, implying the good reusability of the CAG composites. The decreased recycling activity might be due to the shielding of the reactive sites by impurities, and/or structural change of the samples.

Generally, Ag_2CrO_4 is unstable and easily decomposed due to the reduction of Ag^+ and Cr^{6+} under light irradiation. Therefore, the structural stability of CAG composites was evaluated by measuring the high-resolution XPS spectra of Ag 3d and Cr 2p prior and subsequent to photocatalytic reaction [16]. As shown in Fig. 6a, only a doublet peak at 367.8 ($\text{Ag } 3d_{5/2}$) and 373.8 ($\text{Ag } 3d_{3/2}$) eV belonging to Ag^+ can be detected for all composites. Accordingly, the binding energy of Cr^{6+} with the doublet peak at 578.5 ($\text{Cr } 2p_{3/2}$) and 587.7 ($\text{Cr } 2p_{1/2}$) eV was unchanged before and after photocatalytic reaction (Fig. 6b). These results suggest the fact that both Ag^+ and Cr^{6+} are not reduced and the good chemical durability of CA and CAG composites. The further explanation is that CO_2 molecules are more easily reduced than Ag_2CrO_4 and the reduction of CO_2 also protects Ag_2CrO_4 .

The main CO_2 conversion product is CH_3OH , but the samples containing Ag_2CrO_4 also produced a small amount of CH_4 , demonstrating product selectivity. The in-situ FTIR spectra of the CAG composite were

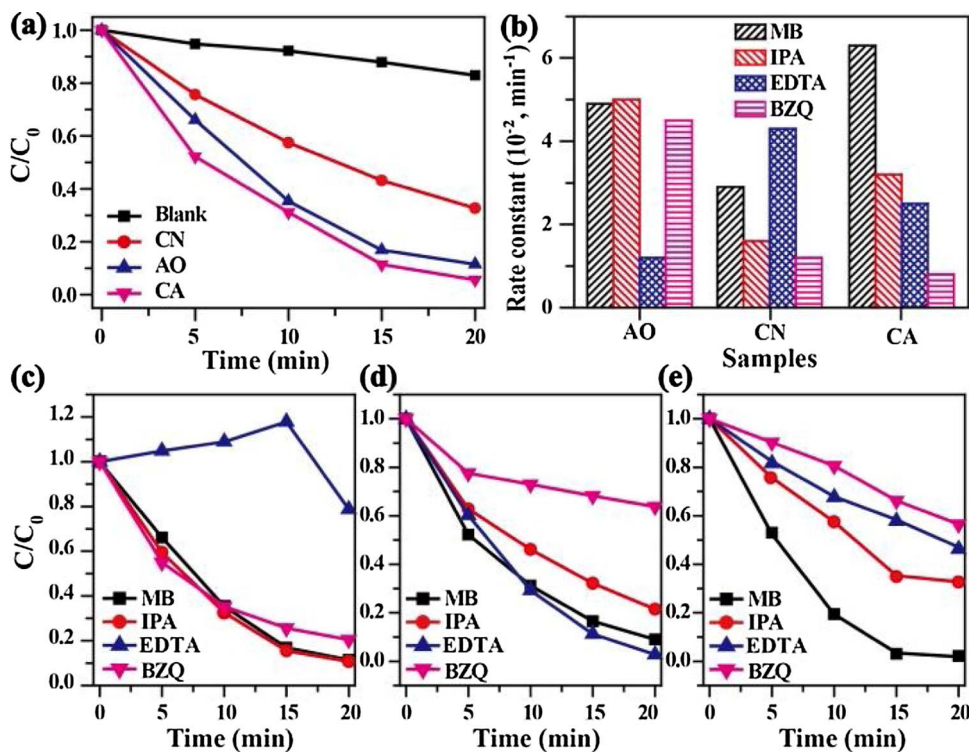


Fig. 8. Comparison on the (a) photocatalytic activity and (b) rate constant of AO, CA and CN samples before and after introducing radical scavengers; radical scavenger test results of (c) AO, (d) CN and (e) CA samples towards MB degradation under visible-light irradiation ($\lambda \geq 400 \text{ nm}$).

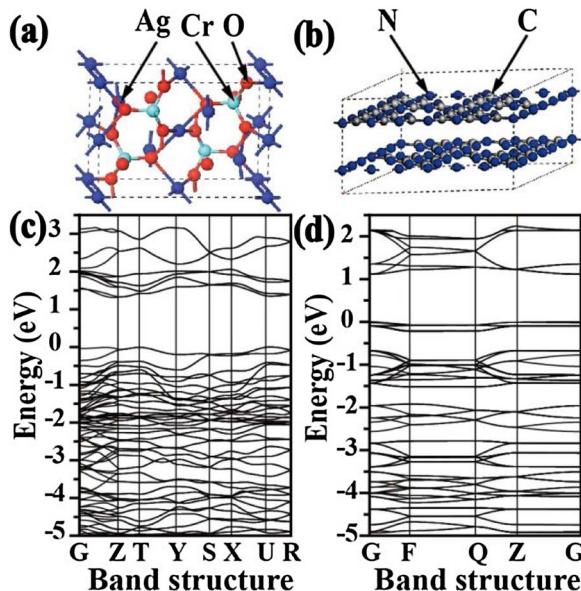


Fig. 9. The crystal structures of (a) Ag_2CrO_4 and (b) $\text{g-C}_3\text{N}_4$, the band structures of (c) Ag_2CrO_4 and (d) $\text{g-C}_3\text{N}_4$.

Table 2

Calculated effective masses of electrons and holes of Ag_2CrO_4 and $\text{g-C}_3\text{N}_4$ by parabolic fitting to the CBM and VBM along specific directions in the reciprocal space.

Samples	$m^* e$				$m^* h$			
	BG	BZ	CG	CZ	UX	UR	CZ	GZ
Ag_2CrO_4	0.50	0.51	0.60	0.67	0.59	0.3	5.21	0.86
$\text{g-C}_3\text{N}_4$	0.48	3.47	13	0.49	0.62	18	13.73	72.8

measured in the dark and under light irradiation to detect the adsorbed and formed species in CO_2 photoreduction process. As shown in Fig. 6c, the bands at 1635 and 1420 cm^{-1} are attributed to monodentate bicarbonate species (HCO_3^-), the bands at 1560 and 1310 cm^{-1} assigned to bidentate carbonate species (b-CO_3^{2-}), and the ones at 1510 and 1350 cm^{-1} attributed to monodentate carbonate species (m-CO_3^{2-}) [7], which all correspond to the adsorbed CO_2 species. After photoreduction for 60 min, the bands derived from the adsorbed CO_2 species decreased and new bands at 1582, 1385 and 1353 cm^{-1} were observed (Fig. 6d), which correspond to the bidentate formate species (COO^-) [7], and increased with increasing irradiation time. This means that formate species are reaction intermediates and the photoreduction process follows the formate multi-electron pathway [1], in which 2, 4, 6 and 8 electrons are required for HCOOH , HCHO , CH_3OH and CH_4 formation, respectively. Therefore, it is not surprising that the reduction of CH_3OH into CH_4 occurred for the CA and CAG samples, because they can provide more electrons with longer lifetime than the CN and CG composites [65].

3.4. Photocatalytic mechanism

Because the CB and VB levels of Ag_2CrO_4 ($E_{\text{CB}} = +0.47 \text{ eV}$, $E_{\text{VB}} = +2.27 \text{ eV}$) are respectively more positive than those of $\text{g-C}_3\text{N}_4$ ($E_{\text{CB}} = -1.3 \text{ eV}$, $E_{\text{VB}} = +1.4 \text{ eV}$) [8,15,16], both type-II and Z-scheme heterojunction mechanisms can be used to explain the charge transfer route between Ag_2CrO_4 and $\text{g-C}_3\text{N}_4$. In the case of type-II heterojunction, photogenerated electrons should transfer from the CB of $\text{g-C}_3\text{N}_4$ to that of Ag_2CrO_4 . Accordingly, Ag^+ should be reduced and CO_2 conversion should be impossible because of the insufficient reduction ability of CB electrons of Ag_2CrO_4 (Fig. 7a), which is distinctly different from the experimental results.

Mott-Schottky measurement shows the n-type semiconductor feature of $\text{g-C}_3\text{N}_4$ and Ag_2CrO_4 , and the flat band potential of $\text{g-C}_3\text{N}_4$ and Ag_2CrO_4 is -1.1 V and $+0.7 \text{ V}$, respectively (Fig. 7b), which approximately corresponds to their Fermi level [66]. Due to the higher Fermi

level of $g\text{-C}_3\text{N}_4$, there is net electron flow from $g\text{-C}_3\text{N}_4$ to Ag_2CrO_4 , and their corresponding Fermi levels are respectively downward and upward shifted until reaching an aligned Fermi energy (E_F) [67]. Accordingly, the bands of $g\text{-C}_3\text{N}_4$ bend upwards while those of Ag_2CrO_4 bend downwards, forming depletion and accumulation layers on the sides of $g\text{-C}_3\text{N}_4$ and Ag_2CrO_4 , respectively. The Fermi level alignment can be demonstrated by the change of relative distance between VB edge level and the Fermi level (E_{VB}). As shown in Fig. 7c, E_{VB} value of CN and CA sample is determined as + 2.0 and + 1.0 eV, respectively, meaning that the Fermi level of the CA composite is shifted towards the VB level compared to $g\text{-C}_3\text{N}_4$ [68]. Consequently, net electrons and holes are gathered on the accumulation layer of Ag_2CrO_4 and the depletion layer of $g\text{-C}_3\text{N}_4$, respectively, which induces an internal electric field (IEF) with a direction from $g\text{-C}_3\text{N}_4$ to Ag_2CrO_4 [69,70] (Fig. 7d).

Under light irradiation, both Ag_2CrO_4 and $g\text{-C}_3\text{N}_4$ are excited, and the IEF drives photogenerated CB electrons of Ag_2CrO_4 to recombine with photogenerated VB holes of $g\text{-C}_3\text{N}_4$, leading to the separation between CB electrons of $g\text{-C}_3\text{N}_4$ and VB holes of Ag_2CrO_4 because this process weakens their Coulomb force. As a result, photogenerated electrons and holes are gathered on the CB of $g\text{-C}_3\text{N}_4$ and VB of Ag_2CrO_4 , respectively. Photogenerated CB electrons of $g\text{-C}_3\text{N}_4$ convert CO_2 into solar fuels such as CH_3OH and CH_4 , while photogenerated VB holes of Ag_2CrO_4 are trapped by water to release O_2 . The above analysis suggests that the CA composite is a direct Z-scheme photocatalyst without any electron mediator such as Ag° (Fig. 7e), which possesses stronger redox ability, higher charge separation efficiency and longer charge carrier lifetime [71]. Moreover, the potential of GO (−0.49 eV, vs. NHE, pH = 7) is lower than that of $g\text{-C}_3\text{N}_4$ [72], thus it is thermodynamically favorable for the photogenerated CB electrons of $g\text{-C}_3\text{N}_4$ to transfer to the surface of GO and then migrate freely along GO conductive network. As a cocatalyst, GO nanosheets not only provide rich adsorption and catalytic sites but also promote electron separation and transport [73,74]. Therefore, the ternary CAG composite exhibited an enhanced photocatalytic CO_2 -conversion activity due to the positive synergistic effect of Ag_2CrO_4 , $g\text{-C}_3\text{N}_4$ and GO.

To further confirm the direct Z-scheme heterojunction mechanism, the radical scavenging experiments of CN, AO and CA samples towards MB degradation were carried out under visible light. The CA sample exhibited the highest photocatalytic activity compared with pristine $g\text{-C}_3\text{N}_4$ and Ag_2CrO_4 (Fig. 8a). For pristine Ag_2CrO_4 , only h_{VB}^+ predominates the photocatalytic activity (Figs. 8b and c), while the reactive species of $g\text{-C}_3\text{N}_4$ are $\cdot\text{O}_2^-$ and $\cdot\text{OH}$ (Fig. 8b and d). For the CA composite, the h_{VB}^+ , $\cdot\text{O}_2^-$ and $\cdot\text{OH}$ are all reactive species towards MB degradation (Fig. 8b and e), suggesting that electrons and holes are gathered on the CB of $g\text{-C}_3\text{N}_4$ and VB of Ag_2CrO_4 , respectively. Undoubtedly, the charge transfer between Ag_2CrO_4 and $g\text{-C}_3\text{N}_4$ follows a direct Z-scheme mechanism, which promotes the separation efficiency, improves the redox ability of charge carriers and thus enhances the photocatalytic CO_2 conversion efficiency.

In addition to the above experimental investigation, the crystal and electronic band structures of Ag_2CrO_4 and $g\text{-C}_3\text{N}_4$ were constructed using DFT calculation (Fig. 9). The effective masses of electrons ($m^* e$) and holes ($m^* h$) along the designated directions are calculated according to Eq. (2) in unit of free-electron mass (m_e), and shown in Table 2. On average, the calculated effective masses of electrons for Ag_2CrO_4 ($\sim 0.51 m_e$) along different directions are much smaller than that of $g\text{-C}_3\text{N}_4$ (e.g., $\sim 0.51 m_e$ vs. $\sim 3.47 m_e$). Considering the faster transfer rate of charge carrier with a smaller effective mass [5], it is more likely that photogenerated electron migration follows the Ag_2CrO_4 -to- $g\text{-C}_3\text{N}_4$ instead of $g\text{-C}_3\text{N}_4$ -to- Ag_2CrO_4 route; the latter is also inhibited by the IEF.

Therefore, the origin of Z-scheme heterojunction of Ag_2CrO_4 / $g\text{-C}_3\text{N}_4$ composites might be due to the following facts. (1) The well-matched band structure between Ag_2CrO_4 and $g\text{-C}_3\text{N}_4$ endows a thermodynamic feasibility for IEF construction and Z-scheme charge separation. (2) The smaller electron effective mass of Ag_2CrO_4 provides a

kinetic possibility for electrons transferring from Ag_2CrO_4 to $g\text{-C}_3\text{N}_4$. (3) The appropriate loading ratio (10 wt%) of Ag_2CrO_4 to $g\text{-C}_3\text{N}_4$ is crucial because the charge transfer route might be switched by the different compositions. For example, Meng et al. reveals that the charge transfer route in Ag_3PO_4 / $g\text{-C}_3\text{N}_4$ composite highly depends on the composition; type-II and Z-scheme heterojunction is formed when the main component is Ag_3PO_4 and $g\text{-C}_3\text{N}_4$, respectively [75]. In this study, an enhanced CO_2 -conversion activity was also obtained with the main component being $g\text{-C}_3\text{N}_4$ instead of Ag_2CrO_4 . (4) The close contact between $g\text{-C}_3\text{N}_4$ and Ag_2CrO_4 with small particle size is important because this can shorten the transfer distance and lower the energy loss of interfacial electron transfer [76].

4. Conclusions

The photocatalytic CO_2 -conversion system over $g\text{-C}_3\text{N}_4$ -based ternary composite photocatalysts containing Ag_2CrO_4 photosensitizer and GO cocatalyst is reported for the first time. The ternary Ag_2CrO_4 / $g\text{-C}_3\text{N}_4$ /GO composite photocatalyst gives a high CO_2 -conversion activity of $1.03 \mu\text{mol g}^{-1}$ with a TOF value of 0.30 h^{-1} under full spectrum simulated sunlight, which is 2.3 times that of pristine $g\text{-C}_3\text{N}_4$. Ag_2CrO_4 nanoparticles employed as photosensitizer can improve the light absorption of $g\text{-C}_3\text{N}_4$, and GO nanosheets serving as electron acceptor can promote charge separation as well as provide plentiful active sites for photocatalytic reduction. More importantly, the charge transfer between Ag_2CrO_4 and $g\text{-C}_3\text{N}_4$ follows a direct Z-scheme mechanism, which not only promotes the charge separation but also improves the redox ability of the photocatalytic system. This work shows a simple way to construct a ternary composite photocatalyst, and provides a new insight to enhance the solar photocatalytic CO_2 -conversion efficiency of $g\text{-C}_3\text{N}_4$ under the synergistic action of Ag_2CrO_4 and GO.

Acknowledgments

This work was supported by NSFC (51320105001, 21573170, 51402025, and 21433007), NSFHP (2015CFA001), Innovative Research Funds of SKLWUT (2017-ZD-4) and the Scientific Research Fund of Hunan Provincial Education Department (16B027).

References

- [1] S.N. Habisreutinger, L. Schmidt-Mende, J.K. Stolarczyk, Photocatalytic reduction of CO_2 on TiO_2 and other semiconductors, *Angew. Chem. Int. Ed* 52 (2013) 7372–7408.
- [2] M. Marszewski, S. Cao, J. Yu, M. Jaroniec, Semiconductor-based photocatalytic CO_2 conversion, *Mater. Horiz.* 2 (2015) 261–278.
- [3] K. Qi, B. Cheng, J. Yu, W. Ho, A review on TiO_2 -based Z-scheme photocatalysts, *Chin. J. Catal.* 38 (2017) 1936–1955.
- [4] Y. Ma, Z. Wang, X. Xu, J. Wang, Review on porous nanomaterials for adsorption and photocatalytic conversion of CO_2 , *Chin. J. Catal.* 38 (2017) 1956–1969.
- [5] W. Yu, D. Xu, T. Peng, Enhanced photocatalytic activity of $g\text{-C}_3\text{N}_4$ for selective CO_2 reduction to CH_3OH via facile coupling of ZnO : a direct Z-scheme mechanism, *J. Mater. Chem. A* 3 (2015) 19936–19947.
- [6] Y. He, L. Zhang, B. Teng, M. Fan, New application of Z-scheme Ag_3PO_4 / $g\text{-C}_3\text{N}_4$ composite in converting CO_2 to fuel, *Environ. Sci. Technol.* 49 (2015) 649–656.
- [7] M. Yamamoto, T. Yoshida, N. Yamamoto, T. Nomoto, Y. Yamamoto, S. Yagi, H. Yoshida, Photocatalytic reduction of CO_2 with water promoted by Ag clusters in $\text{Ag}/\text{Ga}_2\text{O}_3$ photocatalysts, *J. Mater. Chem. A* 3 (2015) 16810–16816.
- [8] X. Wang, S. Blechert, M. Antonietti, Polymeric graphitic carbon nitride for heterogeneous photocatalysis, *ACS Catal.* 2 (2012) 1596–1606.
- [9] S. Cao, J. Low, J. Yu, M. Jaroniec, Polymeric photocatalysts based on graphitic carbon nitride, *Adv. Mater.* 27 (2015) 2150–2176.
- [10] W.J. Ong, L.L. Tan, Y.H. Ng, S.T. Yong, S.P. Chai, Graphitic carbon nitride ($g\text{-C}_3\text{N}_4$)-based photocatalysts for artificial photosynthesis and environmental remediation: are we a step closer to achieving sustainability, *Chem. Rev.* 116 (2016) 7159–7329.
- [11] J. Wen, J. Xie, X. Chen, X. Li, A review on $g\text{-C}_3\text{N}_4$ -based photocatalysts, *Appl. Surf. Sci.* 391 (2017) 72–123.
- [12] J. Fu, J. Yu, C. Jiang, B. Cheng, $g\text{-C}_3\text{N}_4$ -based heterostructured photocatalysts, *Adv. Energy Mater.* 8 (2018) 1701503.
- [13] H. Li, L. Wang, Y. Liu, J. Lei, J. Zhang, Mesoporous graphitic carbon nitride materials: synthesis and modifications, *Res. Chem. Intermed.* 42 (2016) 3979–3998.
- [14] D. Xu, S. Cao, J. Zhang, B. Cheng, J. Yu, Effects of the preparation method on the

structure and the visible-light photocatalytic activity of Ag_2CrO_4 , *Beilstein J. Nanotechnol.* 5 (2014) 658–666.

[15] D. Xu, B. Cheng, S. Cao, J. Yu, Enhanced photocatalytic activity and stability of Z-scheme $\text{Ag}_2\text{CrO}_4\text{-GO}$ composite photocatalysts for organic pollutant degradation, *Appl. Catal. B* 164 (2015) 380–388.

[16] D. Xu, B. Cheng, J. Zhang, W. Wang, J. Yu, W. Ho, Photocatalytic activity of Ag_2MO_4 ($\text{M} = \text{Cr, Mo, W}$) photocatalysts, *J. Mater. Chem. A* 3 (2015) 3–20166.

[17] A. Habibi-Yangjeh, A. Akhundi, Novel ternary $\text{g-C}_3\text{N}_4/\text{Fe}_3\text{O}_4/\text{Ag}_2\text{CrO}_4$ nanocomposites: magnetically separable and visible-light-driven photocatalysts for degradation of water pollutants, *J. Mol. Catal. A* 415 (2016) 122–130.

[18] L. Shi, L. Liang, F. Wang, M. Liu, J. Sun, Ag_2CrO_4 nanoparticles loaded on two-dimensional large surface area graphite-like carbon nitride sheets: simple synthesis and excellent photocatalytic performance, *Dalton Trans.* 45 (2016) 5815–5824.

[19] Y. Shang, X. Chen, W. Liu, P. Tan, H. Chen, L. Wu, C. Ma, X. Xiong, J. Pan, Photocorrosion inhibition and high-efficiency photoactivity of porous $\text{g-C}_3\text{N}_4/\text{Ag}_2\text{CrO}_4$ composites by simple microemulsion-assisted co-precipitation method, *Appl. Catal. B* 204 (2017) 78–88.

[20] J. Luo, X. Zhou, L. Ma, X. Xu, Rational construction of Z-scheme $\text{Ag}_2\text{CrO}_4/\text{g-C}_3\text{N}_4$ composites with enhanced visible-light photocatalytic activity, *Appl. Surf. Sci.* 390 (2016) 357–367.

[21] Y. Deng, L. Tang, G. Zeng, J. Wang, Y. Zhou, J. Wang, J. Tang, Y. Liu, B. Peng, F. Chen, Facile fabrication of a direct Z-scheme $\text{Ag}_2\text{CrO}_4/\text{g-C}_3\text{N}_4$ photocatalyst with enhanced visible light photocatalytic activity, *J. Mol. Catal. A* 421 (2016) 209–221.

[22] P. Zhou, J. Yu, M. Jaroniec, All-solid-state Z-scheme photocatalytic systems, *Adv. Mater.* 26 (2014) 4920–4935.

[23] J. Li, H. Yuan, Z. Zhu, Improved photoelectrochemical performance of Z-scheme $\text{g-C}_3\text{N}_4/\text{Bi}_2\text{O}_3/\text{BiPO}_4$ heterostructure and degradation property, *Appl. Surf. Sci.* 385 (2016) 34–41.

[24] J. Yu, K. Wang, W. Xiao, B. Cheng, Photocatalytic reduction of CO_2 into hydrocarbon solar fuels over $\text{g-C}_3\text{N}_4\text{-Pt}$ nanocomposite photocatalysts, *Phys. Chem. Chem. Phys.* 16 (2014) 11492–11501.

[25] K. Dai, L. Lu, C. Liang, G. Zhu, Q. Liu, L. Geng, J. He, A high efficient graphitic- $\text{C}_3\text{N}_4/\text{BiO}/\text{graphene oxide}$ ternary nanocomposite heterostructured photocatalyst with graphene oxide as electron transport buffer material, *Dalton Trans.* 44 (2015) 7903–7910.

[26] W.K. Jo, N. Clament Sagaya Selvam, Enhanced visible light-driven photocatalytic performance of $\text{ZnO}\text{-g-C}_3\text{N}_4$ coupled with graphene oxide as a novel ternary nanocomposite, *J. Hazard. Mater.* 299 (2015) 462–470.

[27] R.C. Pawar, V. Khare, C.S. Lee, Hybrid photocatalysts using graphitic carbon nitride/cadmium sulfide/reduced graphene oxide ($\text{g-C}_3\text{N}_4/\text{CdS}/\text{RGO}$) for superior photodegradation of organic pollutants under UV and visible light, *Dalton Trans.* 43 (2014) 12514–12527.

[28] T. Ohno, N. Murakami, T. Koyanagi, Y. Yang, Photocatalytic reduction of CO_2 over a hybrid photocatalyst composed of WO_3 and graphitic carbon nitride ($\text{g-C}_3\text{N}_4$) under visible light, *J. CO₂ Util.* 6 (2014) 17–25.

[29] D. Ma, J. Wu, M. Gao, Y. Xin, T. Ma, Y. Sun, Fabrication of Z-scheme $\text{g-C}_3\text{N}_4/\text{RGO}/\text{Bi}_2\text{WO}_6$ photocatalyst with enhanced visible-light photocatalytic activity, *Chem. Eng. J.* 290 (2016) 136–146.

[30] F. Wu, X. Li, W. Liu, S. Zhang, Highly enhanced photocatalytic degradation of methylene blue over the indirect all-solid-state Z-scheme $\text{g-C}_3\text{N}_4\text{-RGO-TiO}_2$ nanoheterojunctions, *Appl. Surf. Sci.* 405 (2017) 60–70.

[31] Q. Xiang, J. Yu, M. Jaroniec, Preparation and enhanced visible-light photocatalytic H_2 -production activity of graphene/ C_3N_4 composites, *J. Phys. Chem. C* 115 (2011) 7355–7363.

[32] Z. Li, J. Wang, K. Zhu, F. Ma, A. Meng, $\text{Ag/g-C}_3\text{N}_4$ composite nanosheets: synthesis and enhanced visible photocatalytic activities, *Mater. Lett.* 145 (2015) 167–170.

[33] L. Cui, X. Ding, Y. Wang, H. Shi, L. Huang, Y. Zuo, S. Kang, Facile preparation of Z-scheme $\text{WO}_3/\text{g-C}_3\text{N}_4$ composite photocatalyst with enhanced photocatalytic performance under visible light, *Appl. Surf. Sci.* 391 (2017) 202–210.

[34] A. Viswanathan, S.A. Suthanthiraraj, Infrared spectroscopic studies of superionic systems $\text{CuI}\text{-Ag}_2\text{XO}_4$ ($\text{X} = \text{Mo, W, Cr}$), *J. Mater. Sci. Lett.* 13 (1993) 1139–1140.

[35] A.B. Laursen, P.C. Veborg, I. Chorkendorff, A high-porosity carbon molybdenum sulphide composite with enhanced electrochemical hydrogen evolution and stability, *Chem. Commun.* 49 (2013) 4965–4967.

[36] H. Cui, Z. Chen, S. Zhong, K.L. Wooley, D.J. Pochan, Block copolymer assembly via kinetic control, *Science* 317 (2007) 647–650.

[37] B. Zhu, L. Zhang, B. Cheng, J. Yu, First-principle calculation study of tri-s-triazine-based $\text{g-C}_3\text{N}_4$: a review, *Appl. Catal. B* 224 (2018) 983–999.

[38] X. Wang, K. Maeda, X. Chen, K. Takanabe, K. Domen, Y. Hou, X. Fu, M. Antonietti, Polymer semiconductors for artificial photosynthesis: hydrogen evolution by mesoporous graphitic carbon nitride with visible light, *J. Am. Chem. Soc.* 131 (2009) 1680–1681.

[39] J.X. Sun, Y.P. Yuan, L.G. Qiu, X. Jiang, A.J. Xie, Y.H. Shen, J.F. Zhu, Fabrication of composite photocatalyst $\text{g-C}_3\text{N}_4\text{-ZnO}$ and enhancement of photocatalytic activity under visible light, *Dalton Trans.* 41 (2012) 6756–6763.

[40] S. Wang, D. Li, C. Sun, S. Yang, Y. Guan, H. He, Synthesis and characterization of $\text{g-C}_3\text{N}_4/\text{Ag}_3\text{VO}_4$ composites with significantly enhanced visible-light photocatalytic activity for triphenylmethane dye degradation, *Appl. Catal. B* 144 (2014) 885–892.

[41] C. Pan, J. Xu, Y. Wang, D. Li, Y. Zhu, Dramatic activity of $\text{C}_3\text{N}_4/\text{BiPO}_4$ photocatalyst with core/shell structure formed by self-assembly, *Adv. Func. Mater.* 22 (2012) 1518–1524.

[42] L. Xin, A. Jin, Y. Jia, T. Xia, C. Deng, M. Zhu, C. Chen, X. Chen, Synergy of adsorption and visible-light photocatalytic degradation of methylene blue by a bi-functional Z-scheme heterojunction of $\text{WO}_3/\text{g-C}_3\text{N}_4$, *Appl. Surf. Sci.* 405 (2017) 359–371.

[43] Y. Gong, X. Quan, H. Yu, S. Chen, Synthesis of Z-scheme $\text{Ag}_2\text{CrO}_4/\text{Ag/g-C}_3\text{N}_4$ composite with enhanced visible-light photocatalytic activity for 2,4-dichlorophenol degradation, *Appl. Catal. B* 219 (2017) 439–449.

[44] B. Zhu, P. Xia, Y. Li, W. Ho, J. Yu, Fabrication and photocatalytic activity enhanced mechanism of direct Z-scheme $\text{g-C}_3\text{N}_4/\text{Ag}_2\text{WO}_4$ photocatalyst, *Appl. Surf. Sci.* 391 (2017) 175–183.

[45] Y. Yang, W. Guo, Y. Guo, Y. Zhao, X. Yuan, Y. Guo, Fabrication of Z-scheme plasmonic photocatalyst $\text{Ag}/\text{AgBr}/\text{g-C}_3\text{N}_4$ with enhanced visible-light photocatalytic activity, *J. Hazard. Mater.* 271 (2014) 150–159.

[46] X. Wang, Y. Liang, W. An, J. Hu, Y. Zhu, W. Cui, Removal of chromium (VI) by a self-regenerating and metal free $\text{g-C}_3\text{N}_4/\text{graphene}$ hydrogel system via the synergy of adsorption and photo-catalysis under visible light, *Appl. Catal. B* 29 (2017) 53–62.

[47] Y. Fu, Z. Li, Q. Liu, X. Yang, H. Tang, Construction of carbon nitride and MoS_2 quantum dot 2D/OD hybrid photocatalyst: Direct Z-scheme mechanism for improved photocatalytic activity, *Chin. J. Catal.* 38 (2017) 2160–2170.

[48] S. Zhou, Y. Liu, J. Li, Y. Wang, G. Jiang, Z. Zhao, D. Wang, A. Duan, J. Liu, Y. Wei, Facile in situ synthesis of graphitic carbon nitride ($\text{g-C}_3\text{N}_4\text{-N-TiO}_2$) heterojunction as an efficient photocatalyst for the selective photoreduction of CO_2 to CO , *Appl. Catal. B* 158–159 (2014) 20–29.

[49] Y. He, Y. Wang, L. Zhang, B. Teng, M. Fan, High-efficiency conversion of CO_2 to fuel over $\text{ZnO}/\text{g-C}_3\text{N}_4$ photocatalyst, *Appl. Catal. B* 168–169 (2015) 1–8.

[50] J. Low, J. Yu, M. Jaroniec, S. Wagh, A.A. Al-Ghamdi, Heterojunction photocatalysts, *Adv. Mater.* 29 (2017) 1601694.

[51] W. Iqbal, B. Tian, M. Anpo, J. Zhang, Single step solvothermal synthesis of mesoporous anatase TiO_2 -reduced graphene oxide nanocomposites for the abatement of organic pollutants, *Res. Chem. Intermed.* 43 (2017) 5187–5201.

[52] K. Wang, Q. Li, B. Liu, B. Cheng, W. Ho, J. Yu, Sulfur-doped $\text{g-C}_3\text{N}_4$ with enhanced photocatalytic CO_2 -reduction performance, *Appl. Catal. B* 176–177 (2015) 44–52.

[53] J. Lei, Y. Chen, F. Shen, L. Wang, Y. Liu, J. Zhang, Surface modification of TiO_2 with $\text{g-C}_3\text{N}_4$ for enhanced UV and visible photocatalytic activity, *J. Alloys Comp.* 631 (2015) 328–334.

[54] D. Tang, G. Zhang, Fabrication of $\text{AgFeO}_2/\text{g-C}_3\text{N}_4$ nanocatalyst with enhanced and stable photocatalytic performance, *Appl. Surf. Sci.* 391 (2017) 415–422.

[55] J. Fu, B. Zhu, C. Jiang, B. Cheng, W. You, J. Yu, Hierarchical porous O-doped $\text{g-C}_3\text{N}_4$ with enhanced photocatalytic CO_2 reduction activity, *Small* 13 (2017) 1603938.

[56] X. Li, J. Yu, S. Wagh, A.A. Al-Ghamdi, J. Xie, Graphene in photocatalysis: a review, *Small* 12 (2016) 6640–6696.

[57] J. Low, Y. Yu, W. Ho, Graphene-based photocatalysts for CO_2 reduction to solar fuel, *J. Phys. Chem. Lett.* 6 (2015) 4244–4251.

[58] B.C. Wood, S.Y. Bhide, D. Dutta, V.S. Kandagal, A.D. Pathak, S.N. Punnathanam, K.G. Ayappa, S. Narasimhan, Methane and carbon dioxide adsorption on edge-functionalized graphene: a comparative DFT study, *J. Chem. Phys.* 137 (2012) 054702.

[59] T. Di, B. Zhu, B. Cheng, J. Yu, J. Xu, A direct Z-scheme $\text{g-C}_3\text{N}_4/\text{SnS}_2$ photocatalyst with superior visible-light CO_2 reduction performance, *J. Catal.* 352 (2017) 532–541.

[60] W. Iqbal, C. Dong, M. Xing, X. Tian, J. Zhang, Eco-friendly one-pot synthesis of well-adorned mesoporous $\text{g-C}_3\text{N}_4$ with efficiently enhanced visible light photocatalytic activity, *Catal. Sci. Technol.* 7 (2017) 1726–1734.

[61] L. Zhou, L. Wang, J. Lei, Y. Liu, J. Zhang, Fabrication of $\text{TiO}_2/\text{Co-g-C}_3\text{N}_4$ heterojunction catalyst and its photocatalytic performance, *Catal. Commun.* 89 (2017) 125–128.

[62] J. Lei, F. Liu, L. Wang, Y. Liu, J. Zhang, A binary polymer composite of graphitic carbon nitride and poly(diphenylbutadiyne) with enhanced visible light photocatalytic activity, *RSC Adv.* 7 (2017) 27377–27383.

[63] P. Niu, Y. Yang, J.C. Yu, G. Liu, H.M. Cheng, Switching the selectivity of the photoreduction reaction of carbon dioxide by controlling the band structure of a $\text{g-C}_3\text{N}_4$ photocatalyst, *Chem. Commun.* 50 (2014) 10837–10840.

[64] Y. Wang, Y. Di, M. Antonietti, H. Li, X. Chen, X. Wang, Excellent visible-light photocatalysis of fluorinated polymeric carbon nitride solids, *Chem. Mater.* 22 (2010) 5119–5121.

[65] J. Jin, J. Yu, G. Guo, C. Cui, W. Ho, A hierarchical Z-scheme CdS-WO_3 photocatalyst with enhanced CO_2 reduction activity, *Small* 11 (2015) 5262–5271.

[66] Y. Yan, H. Guan, S. Liu, R. Jiang, $\text{Ag}_3\text{PO}_4/\text{Fe}_2\text{O}_3$ composite photocatalysts with an $n\text{-}n$ heterojunction semiconductor structure under visible-light irradiation, *Ceram. Int.* 40 (2014) 9095–9100.

[67] J. Yu, J. Low, W. Xiao, P. Zhou, M. Jaroniec, Enhanced photocatalytic CO_2 -reduction activity of anatase TiO_2 by coexposed {001} and {101} facets, *J. Am. Chem. Soc.* 136 (2014) 8839–8842.

[68] W. Iqbal, B. Qiu, J. Lei, L. Wang, J. Zhang, M. Anpo, One-step large-scale highly active $\text{g-C}_3\text{N}_4$ nanosheets for efficient sunlight-driven photocatalytic hydrogen production, *Dalton Trans.* 46 (2017) 10678–10684.

[69] J. Liu, B. Cheng, J. Yu, A new understanding of the photocatalytic mechanism of the direct Z-scheme $\text{g-C}_3\text{N}_4/\text{TiO}_2$ heterostructure, *Phys. Chem. Chem. Phys.* 18 (2016) 31175–31183.

[70] J. Low, C. Jiang, B. Cheng, S. Wagh, A.A. Al-Ghamdi, J. Yu, A review of direct Z-scheme photocatalysts, *Small Methods* 1 (2017) 1700080.

[71] J. Li, M. Zhang, Q. Li, J. Yang, Enhanced visible light activity on direct contact Z-scheme $\text{g-C}_3\text{N}_4\text{-TiO}_2$ photocatalyst, *Appl. Surf. Sci.* 391 (2017) 184–193.

[72] K. Dai, L. Lu, Q. Liu, G. Zhu, X. Wei, J. Bai, L. Xuan, H. Wang, Sonochemical assisted preparation of graphene oxide/graphitic- C_3N_4 nanosheet hybrid with reinforced photocurrent for photocatalyst applications, *Dalton Trans.* 43 (2014) 6295–6299.

[73] H. Yu, P. Xiao, J. Tian, F. Wang, J. Yu, Phenylamine-functionalized rGO/TiO₂ photocatalysts: spatially separated adsorption sites and tunable photocatalytic

selectivity, *ACS Appl. Mater. Interfaces* 8 (2016) 29470–29477.

[74] Y. Xu, Y. Mo, J. Tian, P. Wang, H. Yu, J. Yu, The synergistic effect of graphitic N and pyrrolic N for the enhanced photocatalytic performance of nitrogen-doped graphene/TiO₂ nanocomposites, *Appl. Catal. B* 181 (2016) 810–817.

[75] S. Meng, X. Ning, T. Zhang, S.F. Chen, X. Fu, What is the transfer mechanism of photogenerated carriers for the nanocomposite photocatalyst Ag₃PO₄/g-C₃N₄, band-band transfer or a direct Z-scheme? *Phys. Chem. Chem. Phys.* 17 (2015) 11577–11585.

[76] Q. Xu, J. Yu, J. Zhang, J. Zhang, G. Liu, Cubic anatase TiO₂ nanocrystals with enhanced photocatalytic CO₂ reduction activity, *Chem. Commun.* 51 (2015) 7950–7953.